Nano Research
2021, 14(4): 1195–1201

ISSN 1998-0124 CN 11-5974/O4
https://doi.org/10.1007/s12274-020-3171-4

Research Article

Integrated hetero-nanoelectrodes for plasmon-enhanced electrocatalysis of hydrogen evolution

Wenyu Jiang[1,2], Xianxin Wu[2,3], Jinquan Chang[1,2], Yanhong Ma[1], Luting Song[1], Zhexue Chen[1,2], Cheng Liang[1,2], Xinfeng Liu[2,3], and Yong Zhang[1,2] (✉)

[1] *CAS Key Laboratory of Nanosystem and Hierarchical Fabrication, CAS Center for Excellence in Nanoscience, National Center for Nanoscience and Technology, Beijing 100190, China*
[2] *University of Chinese Academy of Sciences, Beijing 100049, China*
[3] *CAS Key Laboratory of Standardization and Measurement for Nanotechnology, CAS Center for Excellence in Nanoscience, National Center for Nanoscience and Technology, Beijing 100190, China*

Received: 13 July 2020 / **Revised:** 1 October 2020 / **Accepted:** 10 October 2020

ABSTRACT

Hetero-nanostructures of plasmonic metals and semiconductors have attracted increasing attention in the field of photocatalysis. However, most of the hetero-nanostructured catalysts are randomly arranged and therefore require comprehensive structural design for optimizing their properties. Herein, we report the robust construction of hierarchical hetero-nanostructures where gold (Au) nanorods and molybdenum disulfide (MoS_2) quantum sheets (QSs) are integrated in highly ordered arrays. Such construction is achieved through porous anodic alumina (PAA) template-assisted electrodeposition. The as-fabricated hetero-nanostructures demonstrate exciting electrocatalysis towards hydrogen evolution reaction (HER). Both plasmon-induced hot-electron injection and plasmonic scattering/reabsorption mechanisms are determinative to the enhanced electrocatalytic performances. Notably, broadband photoresponses of HER activity in the visible range are observed, indicating their superiority compared with random systems. Such integrated hetero-nanoelectrodes could provide a powerful platform for conversion and utilization of solar energy, meanwhile would greatly prompt the production and exploration of ordered nanoelectrodes.

KEYWORDS

nano-integration, heterostructure, plasmonic metal, molybdenum disulfide (MoS_2), hydrogen evolution reaction (HER)

1 Introduction

Hetero-nanostructures integrating varying nanoscale components have recently attracted much attention thanks to their intrinsic interactions of individual functions (electronic, optical, optoelectronic, catalytic, etc) [1–3]. Such interactions can be further enhanced when the components are orderly arranged in the integrated structures [4]. By precise control of the periodic and structural lengths, the collective behaviors which are not hosted in the individual components can be readily observed [5, 6]. A variety of hetero-nanostructures, such as metal/metal [6–9] and metal/semiconductor [10], have been reported. Notably, the metal/two-dimensional (2D) material hetero-nanostructures [11–13] are emerging for plasmon-enhanced applications in optoelectronics [14], optical sensing [15], and photocatalysis [16]. For example, by combining the plasmonic metal and 2D material catalyst into nanocomposites, enhanced catalytic performances are achieved [17, 18]. However, such randomly mixed structures are lack of sophisticated structural design, which would greatly hinder their potential applications where advanced structures and optimized functions are simultaneously required. Evidently, the hetero-nanostructures with periodicity and hierarchy are highly desired towards integrated functional devices.

The fabrication of hierarchical, periodic hetero-nanostructures often involves state-of-the-art fabrication tools such as lithography. However, the lithographic methods rely on expensive equipment and the as-fabricated structures are usually limited to sub-1 mm length scale, both of which would be problematic for alternative developments where low cost and large area could be primary concern [14, 19]. Many efforts have been made for bridging hetero-nanostructures to macroscale devices. Porous anodic alumina (PAA) templates have been widely utilized for fabrication of hexagonally arranged periodic hetero-nanostructures through electrochemical deposition [6–9] or capillary assembly of colloidal nanoparticles [20].

So far, the metal/2D material hetero-nanostructures have never been fabricated in PAA templates. Herein, we report the robust fabrication of gold-molybdenum disulfide (Au-MoS_2) heterostructured nanorod arrays through PAA template-assisted electrodeposition. The longitudinally segmented Au and MoS_2 nanorods were the plasmonic and catalytic components, respectively. Note that the MoS_2 nanorods were fabricated by direct electrodeposition of the intrinsic and defect-free MoS_2 quantum sheets. Such unique structure enabled the maximum exposure of the MoS_2 catalysts, facilitating the desired catalytic reactions. Compared with randomly dispersed MoS_2 quantum sheets on indium tin oxide (ITO), the as-fabricated Au-MoS_2 nanorod arrays demonstrated significantly enhanced electrocatalytic performances in hydrogen evolution reaction (HER). The HER

Address correspondence to zhangyong@nanoctr.cn

catalysis could be further enhanced under external broadband illumination, indicating exciting photoelectrocatalytic behavior of the integrated hetero-nanoelectrodes. Such plasmon-enhanced electrocatalysis could be driven by both plasmonic hot-electron injection and scattering/reabsorption mechanisms.

2 Results and discussion

Figure 1(a) showed the schematic illustration of the fabrication process for the integrated hetero-nanoelectrodes. The Au thin film was sputtered onto one side of the PAA template (Fig. S1(a) in the Electronic Supplementary Material (ESM)) to form Au-PAA working electrode (Fig. S1(b) in the ESM). By sequential electrodeposition of Au and MoS_2 quantum sheets in PAA, the Au-PAA-Au (Fig. S1(c) in the ESM) and Au-PAA-Au-MoS_2 (Fig. S1(d) in the ESM) hetero-nanostructures were constructed. Note that the Au-PAA-Au-MoS_2 was annealed at 350 °C for 1 hour in argon atmosphere to improve the Au-MoS_2 interfaces and the MoS_2 assembled nanorods. After removal of the PAA templates, the Au-Au-MoS_2 hetero-nanoelectrodes were obtained. Figure 1(b) presented the low-magnification scanning electron microscopy (SEM) image of the hetero-nanoelectrodes, from which highly uniform, high-density integrated structures were observed. High-magnification SEM images were utilized for revealing the microstructure of the hetero-nanoelectrodes. From the top view (Fig. 1(c)), vertically aligned, hexagonally arranged nanorod arrays were identified. Based on the fixed periodic distance of 100 nm, ultrahigh density (approximately 1.1×10^{10} unit/cm^2) of the nanorods was achieved. From the tilted view (Fig. 1(d)), longitudinally segmented Au and MoS_2 nanorods were clearly identified from their light and dark contrast, respectively. Note that the Au-Au (film-nanorod) contacts were partially broken by sonication

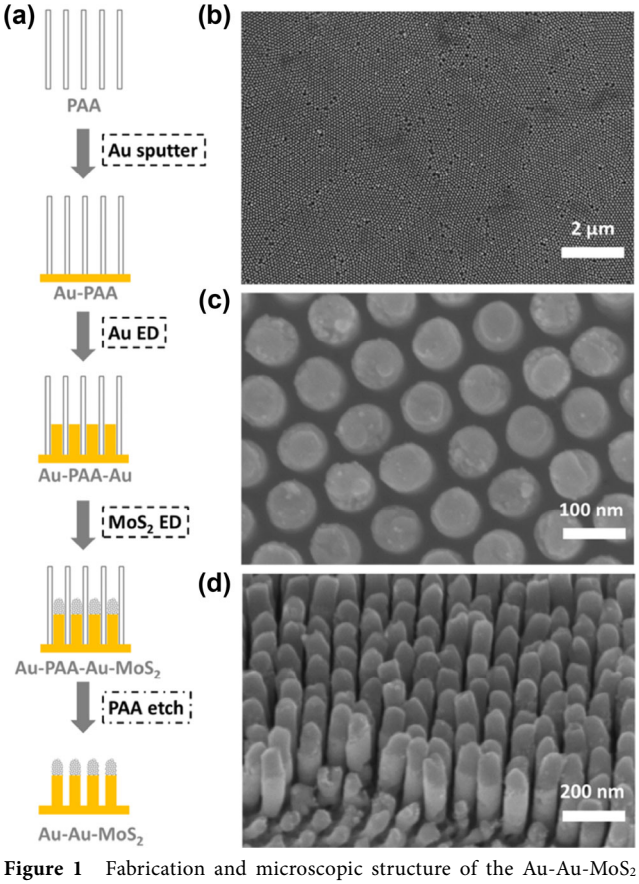

Figure 1 Fabrication and microscopic structure of the Au-Au-MoS_2 integrated hetero-nanoelectrodes. (a) Schematic illustration of the fabrication process. (b) and (c) Top-view and (d) tilted-view SEM images.

treatment for complete exposure (facilitating the observation) of the Au-Au-MoS_2 hetero-nanoelectrodes. Such integrated structures enabled sophisticated structural design in terms of segmental materials, lengths, and diameters [21]. The crystal structures of the Au-MoS_2 hetero-nanorods (i.e., units of the integrated electrodes) were revealed with transmission electron microscopy (TEM) and high-resolution TEM (HRTEM). Figure S4(c) in the ESM showed the TEM image of a representative single hetero-nanorod (after annealing), in which the Au and MoS_2 segments were resolved by their dark and light contrast, respectively. Figure S4(d) in the ESM presented the HRTEM image of the Au-MoS_2 interface (after annealing) where the compact, distinct hetero-junction was observed. In the Au segment, clear lattices were observed with the spacing of 0.23 nm corresponding to the (111) plane of Au. While in the MoS_2 segment, polycrystalline structures were identified and confirmed by the fast Fourier transform (FFT) pattern. The lattice fringes with an interplanar spacing of 0.27 nm corresponded to the (100) lattice planes of MoS_2. As shown in Figs. S4(a) and S4(b) in the ESM, relatively loose MoS_2 segment and Au-MoS_2 interface were detected in the hetero-nanorod before annealing. Evidently, the annealing process was crucial to obtain improved structures of both MoS_2 segment and Au-MoS_2 interface, which would facilitate the charge transfer across MoS_2 and between Au and MoS_2. Meanwhile, the assembled nature of the MoS_2 nanorod was firmly supported by the TEM and HRTEM images. After annealing, the assembled nature (with sub-2 nm gaps) remained, facilitating the examined catalytic reactions. As stated above, the MoS_2 nanorods were formed through electrodeposition of the MoS_2 quantum sheets which were obtained based on our recent reports [22, 23]. Such unique MoS_2 nanorods had never been reported before, which could be extended to other types of 2D materials [23]. The MoS_2 quantum sheets were 2–3 nm in lateral sizes (Figs. S3(a), S3(b) and S3(c) in the ESM) and 1–2 layers in thicknesses, much smaller than the PAA pores (80 nm) (Fig. S1(a) in the ESM). Besides, the MoS_2 quantum sheets showed satisfactory stability in water with the negative zeta potential of −31.7 mV (at 0.1 mg/mL). Such features ensured the successful electrodeposition of the MoS_2 quantum sheets into the PAA templates. Detailed information of the MoS_2 quantum sheets could be found in our recent work [23].

The as-fabricated Au-Au-MoS_2 integrated hetero-nanoelectrodes were optically/spectroscopically characterized. Figure 2(a) showed the optical images of the Au-Au (Au nanorod arrays on the Au film, without PAA) and Au-Au-MoS_2 structures, respectively. Compared with the Au-Au, the Au-Au-MoS_2 exhibited apparently dark color, indicating its enhanced absorption of the light. Such direct observation was confirmed by the evolution of their extinction spectra, as presented in Fig. 2(b). Two characteristic peaks at 595 and 707 nm were detected in the spectrum of the Au-Au, corresponding to the transverse and longitudinal modes of the surface plasmon resonances (SPR) of the Au nanorods (with diameters and lengths of 80 and 240 nm, Fig. S1(d) in the ESM), respectively [24]. However, the longitudinal SPR red-shifted (by 18 nm) to 725 nm in the spectrum of the Au-Au-MoS_2, indicating the existence of the Au-MoS_2 interactions [17, 18, 25]. Besides the characteristic peak shifting, the absorption in the visible range was greatly increased in the Au-Au-MoS_2 compared with the Au-Au. The deposition of the MoS_2 quantum sheets onto the Au nanorods would be responsible to the improvement in absorption. Meanwhile, the as-formed MoS_2 nanorods (with lengths of 120 nm, Fig. S1(d) in the ESM) could demonstrate enhanced absorption compared with the dispersed MoS_2 quantum sheets [23]. Such broadband, strong absorption in

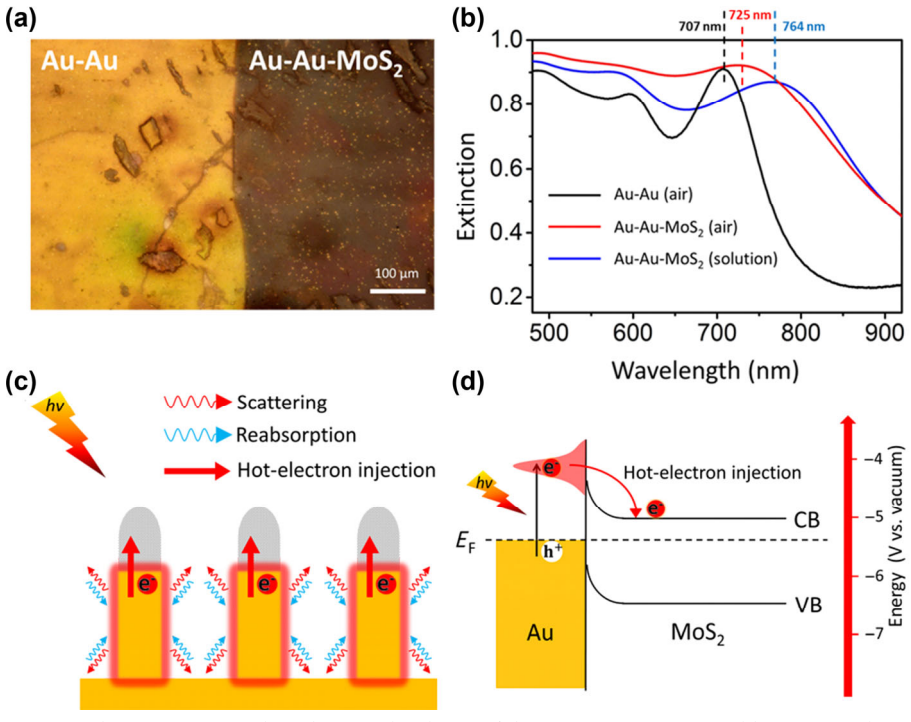

Figure 2 Optical/spectroscopic characterization and mechanism elucidation of the Au-Au-MoS_2 integrated hetero-nanoelectrodes. (a) Optical images and (b) extinction spectra of the Au-Au and Au-Au-MoS_2 structures. Schematic illustration of (c) plasmon-enhanced light-matter interactions and (d) plasmon-induced hot-electron injection.

the visible range for the Au-Au-MoS_2 could be driven by the plasmon-enhanced light-matter interactions, as shown in Fig. 2(c). Two mechanisms were proposed for the light-matter interactions in the Au-Au-MoS_2. One involved the plasmonic scattering/reabsorption and the other indicated the plasmon-induced hot-electron injection. The relatively large (e.g., > 60 nm) Au nanorods could efficiently scatter the resonant photons [11, 26–28], which would significantly increase the path length of photons in the Au-Au-MoS_2. The scattered photons could be reabsorbed by the adjacent Au and MoS_2 nanorods therefore improved the light absorption of the Au-Au-MoS_2. Considering the deep subwavelength gaps (20 nm) between nanorods, the transverse SPR coupling could be very strong [20], ensuring the desired light-trapping in the arrays. Such light-trapping promised sufficient light scattering/reabsorption, resulting in enhanced absorption in the Au-Au-MoS_2. The plasmon-induced hot-electron injection could contribute to the absorption enhancement as well. From Fig. 2(d), when the plasmon-induced hot electrons were injected from Au to MoS_2, the excited plasmons would be relaxed. Such non-radiative relaxation of SPR would evidently improve the light absorption [11]. Meanwhile, the electron transfer between Au and MoS_2 could be determinative to the examined catalytic reactions (see the following section). The interactions between Au and MoS_2 were also supported by Raman spectroscopy (Fig. S5 in the ESM), in which both E^1_{2g} and A_{1g} modes in the Au-MoS_2 red-shifted compared with the MoS_2 quantum sheets [23, 29, 30]. Considering that the HER measurements were conducted in aqueous solution, the extinction spectra of the Au-Au-MoS_2 were measured in solution as well. From Fig. 2(b), the longitudinal SPR in solution red-shifted to 764 nm, probably because of the relatively large dielectric functions of the aqueous solution compared with those of the air [24]. In addition, the X-ray photoelectron spectroscopy (XPS) measurements were conducted to further illustrate the electron transfer. From the XPS spectra (Fig. S6 in the ESM), the binding energy of Mo $3d_{3/2}$ and Mo $3d_{5/2}$ in Au-Au-MoS_2 heterostructure negatively shifted by 0.22 and 0.35 eV respectively, compared with those in MoS_2 QSs. Similarly, S $2p_{1/2}$ and S $2p_{3/2}$ in the heterostructure showed lower binding energy (negatively shifted by 0.29 and 0.41 eV respectively) than those in MoS_2 QSs. However, the binding energy of Au $4f_{5/2}$ and Au $4f_{7/2}$ in Au-Au-MoS_2 positively shifted by 0.28 and 0.25 eV respectively compared with those in Au-Au. Further, the intensity ratio of Mo $3d_{3/2}$ and Mo $3d_{5/2}$ in Au-Au-MoS_2 was evidently different from that in MoS_2 QSs. These results all suggested the electron transfer from Au to MoS_2 [17].

The exceptional absorption behavior of the Au-Au-MoS_2 could greatly facilitate its plasmon-enhanced applications. As a demonstration, the HER electrocatalytic performances of the Au-Au-MoS_2 were evaluated in this work. Current research on the Au/MoS_2 catalysts was far from satisfactory, largely because of their random structures [17, 18, 30–33]. The Au-Au-MoS_2 was fabricated as the hierarchical, periodic integrated hetero-nanoelectrodes where the Au, Au, and MoS_2 functioned as the supporting conductive film, plasmon generator, and electrocatalyst, respectively. Figure S7 in the ESM showed the schematic illustration of the typical three-electrode configuration (the Au-Au-MoS_2 as the working electrode) for the HER measurements. Detailed information of the HER measurements could be found in the ESM. From Fig. 3(a), both Au film and MoS_2 quantum sheets on ITO showed negligible HER activity. The Au-Au presented improved HER performance with the η_{onset} (onset overpotential) and η_{10} (overpotential at the current density of 10 mA/cm^2) at –0.24 and –0.36 V respectively. Such improvement could be related with the formation of sub-wavelength nanorod arrays with increased specific surface areas (Fig. S2 in the ESM). Compared with the Au-Au structure, the Au-Au-MoS_2 hetero-nanoelectrodes demonstrated significantly enhanced HER performance with the η_{onset} and η_{10} at –0.15 and –0.28 V respectively. The as-deposited MoS_2 nanorods could be responsible to the enhancement of the HER performance. With the annealed Au-Au-MoS_2, the η_{10} positively shifted to –0.26 V, while the η_{onset} remained unchanged. When irradiated with the 721 nm (comparable to the longitudinal SPR wavelength of

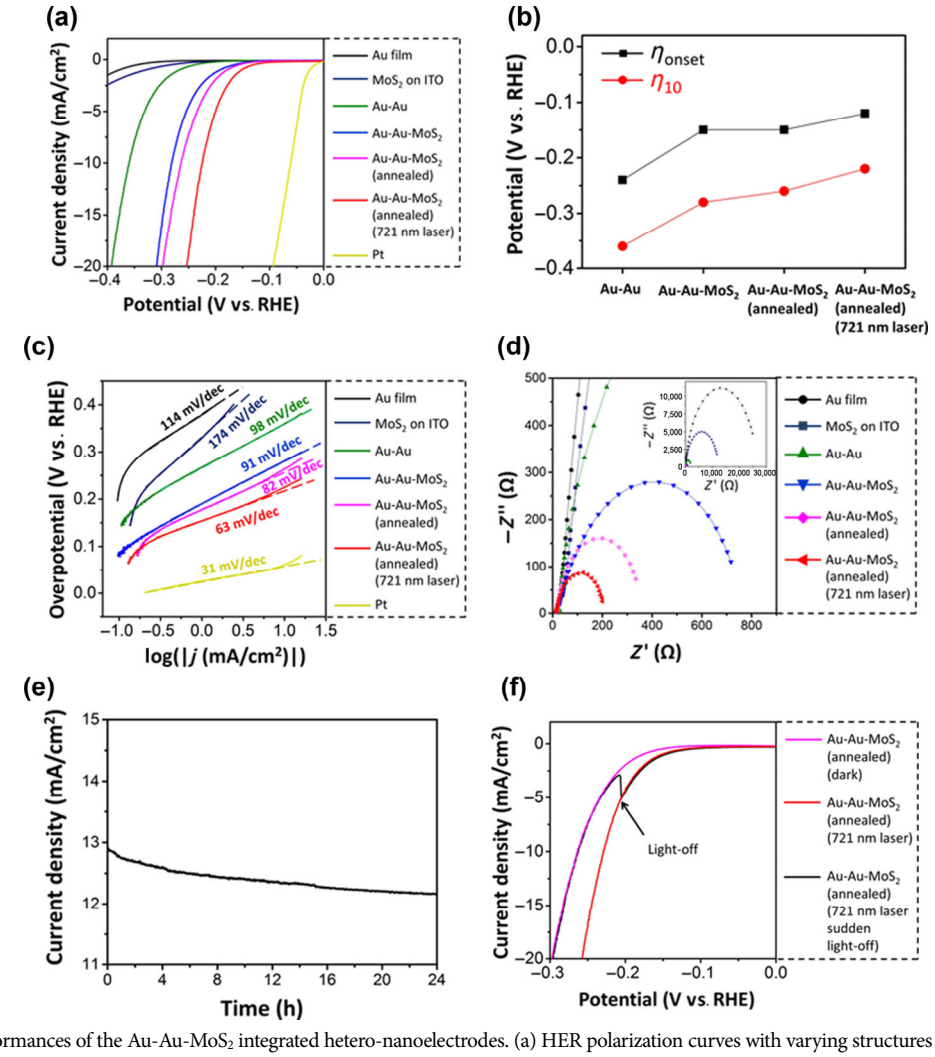

Figure 3 HER performances of the Au-Au-MoS_2 integrated hetero-nanoelectrodes. (a) HER polarization curves with varying structures and states. (b) Evolution of the η_{onset} and η_{10} with varying structures and states. (c) Tafel plots and slopes derived from the polarization curves. (d) EIS spectra with varying structures and states. (e) Stability test for the Au-Au-MoS_2 electrode. (f) Photoresponses of the Au-Au-MoS_2 electrode.

the integrated hetero-nanoelectrodes) laser (1 W/cm^2), the HER activity of the (annealed) Au-Au-MoS_2 was remarkably increased. The η_{onset} and η_{10} at –0.12 and –0.22 V respectively were achieved, indicating exciting photoelectrocatalysis in HER. The evolution of the η_{onset} and η_{10} with varying structures and states was shown in Fig. 3(b). Such evolution clearly demonstrated the determinative roles of the integrated hetero-nanoelectrodes and the plasmon-enhanced electrocatalysis of HER. To better understand the electrode reaction kinetics and mechanism, Tafel plots and slopes were derived from the polarization curves in Fig. 3(a). As shown in Fig. 3(c), high Tafel slopes (e.g., > 100 mV/dec) indicated that the Volmer step was the rate-determining step. Similar trends were found in both evolutions of the potentials and the slopes. Particularly, the Tafel slope of the (annealed) Au-Au-MoS_2 was decreased from 82 to 63 mV/dec when the 721 nm (near resonance) laser was illuminated on the sample. The decrease of Tafel slope suggested that Volmer reaction was no longer the only determinative step, meanwhile confirmed the plasmon-enhanced (accelerated) electrocatalysis of HER. The reaction kinetics was further explored by the electrochemical impedance spectroscopy (EIS), as shown in Fig. 3(d) and Table S1 in the ESM. The large radii of the spectra of Au film, MoS_2 on ITO, and Au-Au indicated the high charge transfer resistance in reaction. However, the Au-Au-MoS_2 showed much lower charge transfer resistance of approximately 780 Ω than its individual components (e.g., Au film, Au-Au, and MoS_2 on ITO). When annealed, the charge transfer resistance was decreased to approximately 350 Ω. These results confirmed that the annealing process could improve the interfaces between Au and MoS_2 thus facilitate the electron transfer. Notably, the charge transfer resistance of the annealed Au-Au-MoS_2 was further decreased to approximately 210 Ω when illuminated with 721 nm laser, which supported that the plasmon-induced hot electrons would cause higher charge transport efficiency in the electrode.[34] In addition, the Mott-Schottky plots were measured to investigate the flat-band potentials (V_{fb}) of the annealed Au-Au-MoS_2 with and without 721 nm laser illumination. From Fig. S9 in the ESM, the positive slopes of the curves indicated the n-type characteristic of the Au-Au-MoS_2. The flat-band potential (equal to Fermi level, E_f, for n-type semiconductors) was determined to be –0.303 V (vs. NHE) in the dark, while it was shifted to –0.366 V (vs. NHE) under 721 nm laser illumination. Such shift of flat-band potential (equal to E_f) under illumination was a solid evidence for continuous electron transfer from Au to MoS_2 [34]. From the above, the enhancement/acceleration could be explained as follows. In the Au-Au-MoS_2 integrated hetero-nanoelectrodes, the Schottky barriers at the Au-MoS_2 junctions blocked the electron transfer from Au to MoS_2. However, the near-resonance laser illumination enabled the (longitudinal) plasmonic excitation. The excited plasmons could decay non-radiatively by transferring their energies to the energetic charge carriers (i.e., hot electrons and holes) [35]. The hot electrons with energies high enough to overcome the Schottky barriers

were then injected into the conduction band of the MoS_2, ensuring satisfactory conductivity for the desired chemical reactions [36–38]. Meanwhile, the excited plasmons could decay radiatively as well by scattering of the resonant photons [35]. The scattered photons were then reabsorbed by the adjacent nanorods, improving the light utilization. Both plasmonic scattering/reabsorption and plasmon-induced hot-electron injection mechanisms (Figs. 2(c) and 2(d)) could be responsible to the observed plasmon-enhanced electrocatalysis of HER. Figure 3(e) showed the stability of the electrode. At overpotential of −0.22 V, the current density remained relatively stable (~ 12 mA/cm^2) over 24 h with an acceptable loss of 5.8%. To testify the photoresponses of the integrated hetero-nanoelectrodes, the linear sweep voltammetry (LSV) measurement with the laser (721 nm, 1 W/cm^2) on and off was conducted. As shown in Fig. 3(f), when the laser was blocked (at −0.2 V) during the scanning, the polarization current would abruptly drop to its dark state. Such instant dropping in current was attributed to the photoelectrocatalytic rather than photothermal effect (gradual dropping) [34, 39].

To systematic investigate the photoresponses of the HER performances of the Au-Au-MoS_2 integrated hetero-nanoelectrodes, the chronoamperometric (CA) curves (at −0.2 V) with varying structures and states were recorded. Figure 4(a) showed the CA curves with alternating 721 nm laser (1 W/cm^2) on/off states. The MoS_2 quantum sheets on ITO exhibited almost no response to the 721 nm laser illumination, while other structures with Au components presented switchable, stable photoresponses, identifying the determinative role of Au in the plasmon-enhanced electrocatalysis. Compared with the Au film and the Au-Au, the Au-Au-MoS_2 demonstrated remarkably enhanced photoresponses to the 721 nm (near-resonance) laser, supporting the proposed mechanisms in Figs. 2(c) and 2(d). In addition, the annealed Au-Au-MoS_2 showed much higher photoresponses than the unannealed, which could be resulted from the improved Au-MoS_2 interfaces by annealing (facilitating the plasmon-induced hot-electron injection). Figure 4(b) presented the CA curves of the (annealed) Au-Au-MoS_2 with varying laser (fixed at 1 W/cm^2) wavelengths. Evidently, the Au-Au-MoS_2 demonstrated broadband, switchable photoresponses thanks to its strong absorption of the visible light (Fig. 2(b)). The photoresponses were steadily improved with the increasing wavelengths and reached the maximum when illuminated with the 721 nm (near the longitudinal resonance) laser. However, the photoresponse with the 946 nm laser was greatly suppressed due to the dramatically decreased absorption in the near infrared (IR) range (Fig. 2(b)). Such broadband photoresponses of the HER performances were further confirmed by utilizing the white light (1 W/cm^2) illumination (Fig. S10 in the ESM). From Fig. 4(c), the Au-Au-MoS_2 showed satisfactory photoresponse under white light, comparable to that under 721 nm laser, facilitating its practical applications in photoelectrocatalysis. The broadband photoresponses of the HER activity of the Au-Au-MoS_2 integrated hetero-nanoelectrodes were beyond the capacity of the random Au/MoS_2 structures [17]. Such photoelectrocatalysis in hierarchical, periodic hetero-nanostructures (Fig. 4(d)) would boost the mass production and full exploration of ordered nanoelectrodes.

3 Conclusions

In summary, we have presented the Au-Au-MoS_2 integrated hetero-nanoelectrodes where the longitudinally segmented Au and MoS_2 nanorods were vertically aligned, hexagonally arranged on the conductive Au film. This was achieved through sequential electrodeposition of the Au and MoS_2 quantum sheets into the PAA template. The Au-Au-MoS_2 showed broadband, strong absorption in the visible range, which could be driven by both plasmonic scattering/reabsorption and plasmon-induced hot-electron injection mechanisms. Such unique absorption behavior enabled the broadband, switchable, and stable photoresponses of the HER performances of the Au-Au-MoS_2. The plasmon-enhanced electrocatalysis could be readily manipulated by either laser or white light illumination, facilitating their practical

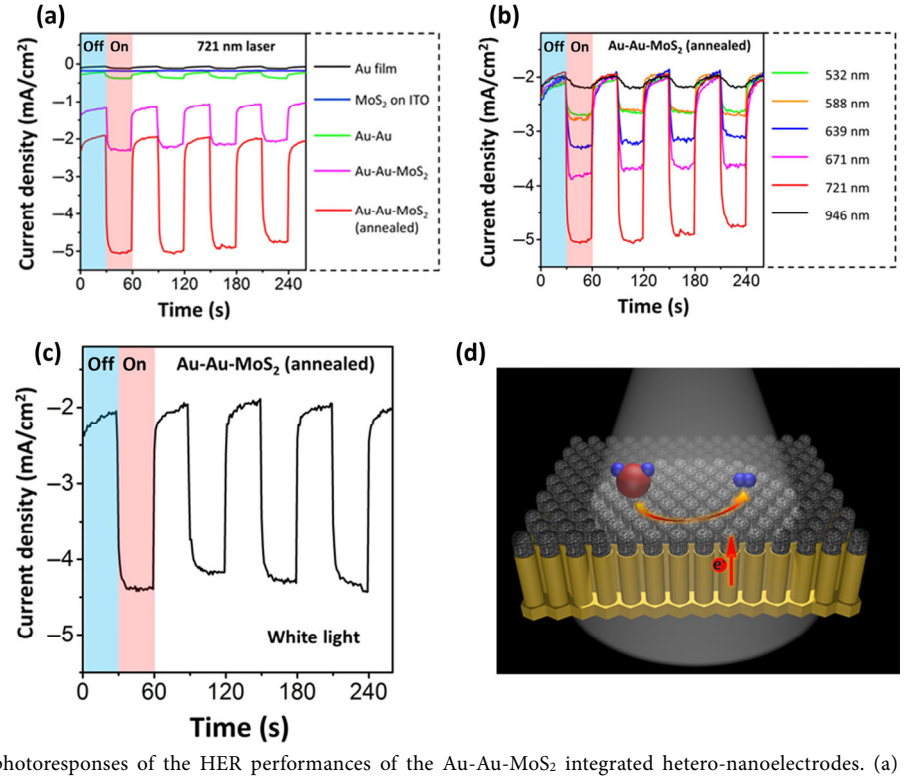

Figure 4 Broadband photoresponses of the HER performances of the Au-Au-MoS_2 integrated hetero-nanoelectrodes. (a) Structure-determined, (b) laser-dependent, and (c) white-light-excited, photoresponsive CA curves (at −0.2 V). (d) Schematic illustration of the photoelectrocatalysis in HER.

applications in photoelectrocatalysis. Our work would open new avenues towards the design and development of hierarchical, periodic nanoelectrodes for solar energy conversion and utilization.

Acknowledgements

This work was supported by the National Natural Science Foundation of China (Nos. 61575049, 51601046, 51802054, 21673054, and 11874130), Strategic Priority Research Program of Chinese Academy of Sciences (No. XDB36000000), the National Key R&D Program of China (No. 2018YFA0703700), Open Research Fund Program of the State Key Laboratory of Low-Dimensional Quantum Physics (KF201902), and start-up funding from National Center for Nanoscience and Technology.

Electronic Supplementary Material: Supplementary material (experimental details and additional data) is available in the online version of this article at https://doi.org/10.1007/s12274-020-3171-4.

References

[1] Begley, M. R.; Gianola, D. S.; Ray, T. R. Bridging functional nanocomposites to robust macroscale devices. *Science* **2019**, *364*, eaav4299.

[2] Jiang, R. B.; Li, B. X.; Fang, C. H.; Wang, J. F. Metal/semiconductor hybrid nanostructures for plasmon-enhanced applications. *Adv. Mater.* **2014**, *26*, 5274–5309.

[3] Tan, H. L.; Abdi, F. F.; Ng, Y. H. Heterogeneous photocatalysts: An overview of classic and modern approaches for optical, electronic, and charge dynamics evaluation. *Chem. Soc. Rev.* **2019**, *48*, 1255–1271.

[4] Liang, X. G.; Dong, R. T0; Ho, J. C. Self-assembly of colloidal spheres toward fabrication of hierarchical and periodic nanostructures for technological applications. *Adv. Mater. Technol.* **2019**, *4*, 1800541.

[5] Hsueh, H. Y.; Yao, C. T.; Ho, R. M. Well-ordered nanohybrids and nanoporous materials from gyroid block copolymer templates. *Chem. Soc. Rev.* **2015**, *44*, 1974–2018.

[6] Zhang, Y.; Ashall, B.; Doyle, G.; Zerulla, D.; Lee, G. U. Highly ordered Fe-Au heterostructured nanorod arrays and their exceptional near-infrared plasmonic signature. *Langmuir* **2012**, *28*, 17101–17107.

[7] Ma, Y. H.; Jiang, W. Y.; Xu, Y. Q.; Zhang, Y. Multisegmented metallic nanorods: Sub-10 nm growth, nanoscale manipulation, and subwavelength imaging. *Adv. Mater.* **2019**, *31*, 1804958.

[8] Zhang Y.; Wang, Q.; Ashall, B.; Zerulla, D.; Lee, G. U. Magnetic-plasmonic dual modulated FePt-Au ternary heterostructured nanorods as a promising nano-bioprobe. *Adv. Mater.* **2012**, *24*, 2485–2490.

[9] Zhang, Y.; DaSilva, M.; Ashall, B.; Doyle, G.; Zerulla, D.; Sands, T. D.; Lee, G. U. Magnetic manipulation and optical imaging of an active plasmonic single-particle Fe-Au nanorod. *Langmuir* **2011**, *27*, 15292–15298.

[10] Valenti, M.; Jonsson, M. P.; Biskos, G.; Schmidt-Ott, A.; Smith, W. A. Plasmonic nanoparticle-semiconductor composites for efficient solar water splitting. *J. Mater. Chem. A* **2016**, *4*, 17891–17912.

[11] Li, X. H.; Zhu, J. M.; Wei, B. Q. Hybrid nanostructures of metal/two-dimensional nanomaterials for plasmon-enhanced applications. *Chem. Soc. Rev.* **2016**, *45*, 3145–3187.

[12] Hong, M.; Shi, J. P.; Huan, Y. H.; Xie, Q.; Zhang, Y. F. Microscopic insights into the catalytic mechanisms of monolayer MoS_2 and its heterostructures in hydrogen evolution reaction. *Nano Res.* **2019**, *12*, 2140–2149.

[13] Sun, Y. H.; Zhao, H. F.; Zhou, D.; Zhu, Y. C.; Ye, H. Y.; Moe, Y. A.; Wang, R. M. Direct observation of epitaxial alignment of Au on MoS_2 at atomic resolution. *Nano Res.* **2019**, *12*, 947–954.

[14] Jang, S.; Hwang, E.; Lee, Y.; Lee, S.; Cho, J. H. Multifunctional graphene optoelectronic devices capable of detecting and storing photonic signals. *Nano Lett.* **2015**, *15*, 2542–2547.

[15] Lee, B.; Park, J.; Han, G. H.; Ee, H. S.; Naylor, C. H.; Liu, W. J.; Johnson, A. T. C.; Agarwal, R. Fano resonance and spectrally modified photoluminescence enhancement in monolayer MoS_2 integrated with plasmonic nanoantenna Array. *Nano Lett.* **2015**, *15*, 3646–3653.

[16] Yin, Z. Y.; Chen, B.; Bosman, M.; Cao, X. H.; Chen, J. Z.; Zheng, B.; Zhang, H. Au nanoparticle-modified MoS_2 nanosheet-based photoelectrochemical cells for water splitting. *Small* **2014**, *10*, 3537–3543.

[17] Shi, Y.; Wang, J.; Wang, C.; Zhai, T. T.; Bao, W. J.; Xu, J. J.; Xia, X. H.; Chen, H. Y. Hot electron of Au nanorods activates the electrocatalysis of hydrogen evolution on MoS_2 nanosheets. *J. Am. Chem. Soc.* **2015**, *137*, 7365–7370.

[18] Zhang, P.; Fujitsuka, M.; Majima, T. Hot electron-driven hydrogen evolution using anisotropic gold nanostructure assembled monolayer MoS_2. *Nanoscale* **2017**, *9*, 1520–1526.

[19] Lin, Q. Y.; Mason, J. A.; Li, Z. Y.; Zhou, W. J.; O'Brien, M. N.; Brown, K. A.; Jones, M. R.; Butun, S.; Lee, B.; Dravid, V. P. et al. Building superlattices from individual nanoparticles via template-confined DNA-mediated assembly. *Science* **2018**, *359*, 669–672.

[20] Jiang, W. Y.; Ma, Y. H.; Zhao, J.; Li, L. L.; Xu, Y. Q.; Guo, H. B.; Song, L. T.; Chen, Z. X.; Zhang, Y. Robust assembly of colloidal nanoparticles for controlled-reflectance surface construction. *ACS Appl. Mater. Interfaces* **2019**, *11*, 23773–23779.

[21] Zhang, Y.; Wang, J. J.; Ballantine, K. E.; Eastham, P. R.; Blau, W. J. Hybrid plasmonic nanostructures with unconventional nonlinear optical properties. *Adv. Opt. Mater.* **2014**, *2*, 331–337.

[22] Han, C. C.; Zhang, Y.; Gao, P.; Chen, S. L.; Liu, X. F.; Mi, Y.; Zhang, J. Q.; Ma, Y. H.; Jiang, W. Y.; Chang, J. Q. High-yield production of MoS_2 and WS_2 quantum sheets from their bulk materials. *Nano Lett.* **2017**, *17*, 7767–7772.

[23] Xu, Y. Q.; Chen, S. L.; Dou, Z. P.; Ma, Y. H.; Mi, Y.; Du, W. N.; Liu, Y.; Zhang, J. Q.; Chang, J. Q.; Liang, C. et al. Robust production of 2D quantum sheets from bulk layered materials. *Mater. Horiz.* **2019**, *6*, 1416–1424.

[24] Kabashin, A. V.; Evans, P.; Pastkovsky, S.; Hendren, W.; Wurtz, G. A.; Atkinson, R.; Pollard, R.; Podolskiy, V. A.; Zayats, A. V. Plasmonic nanorod metamaterials for biosensing. *Nat. Mater.* **2009**, *8*, 867–871.

[25] Li, Y.; Cain, J. D.; Hanson, E. D.; Murthy, A. A.; Hao, S. Q.; Shi, F. Y.; Li, Q. Q.; Wolverton, C.; Chen, X. Q.; Dravid, V. P. Au@MoS_2 core-shell heterostructures with strong light-matter interactions. *Nano Lett.* **2016**, *16*, 7696–7702.

[26] Zhang, P.; Wang, T.; Gong, J. L. Mechanistic understanding of the plasmonic enhancement for solar water splitting. *Adv. Mater.* **2015**, *27*, 5328–5342.

[27] Mascaretti, L.; Dutta, A.; Kment, Š.; Shalaev, V. M.; Boltasseva, A.; Zboril, R.; Naldoni, A. Plasmon-enhanced photoelectrochemical water splitting for efficient renewable energy storage. *Adv. Mater.* **2019**, *31*, 1805513.

[28] Zhang, X. M.; Chen, Y. L.; Liu, R. S.; Tsai, D. P. Plasmonic photocatalysis. *Rep. Prog. Phys.* **2013**, *76*, 046401.

[29] Sreeprasad, T. S.; Nguyen, P.; Kim, N.; Berry, V. Controlled, defect-guided, metal-nanoparticle incorporation onto MoS_2 via chemical and microwave routes: Electrical, thermal, and structural properties. *Nano Lett.* **2013**, *13*, 4434–4441.

[30] Kang, Y. M.; Gong, Y. L.; Hu, Z. J.; Li, Z. W.; Qiu, Z. W.; Zhu, X.; Ajayan, P. M.; Fang, Z. Plasmonic hot electron enhanced MoS_2 photocatalysis in hydrogen evolution. *Nanoscale* **2015**, *7*, 4482–4488.

[31] Shi, J. P.; Ma, D. L.; Han, G. F.; Zhang, Y.; Ji, Q. Q.; Gao, T.; Sun, J. Y.; Song, X. J.; Li, C.; Zhang, Y. S. et al. Controllable growth and transfer of monolayer MoS_2 on Au foils and its potential application in hydrogen evolution reaction. *ACS Nano* **2014**, *8*, 10196–10204.

[32] Wang, T. Y.; Liu, L.; Zhu, Z. W.; Papakonstantinou, P.; Hu, J. B.; Liu, H. Y.; Li, M. X. Enhanced electrocatalytic activity for hydrogen evolution reaction from self-assembled monodispersed molybdenum sulfidenanoparticles on an Au electrode. *Energy Environ. Sci.* **2013**, *6*, 625–633.

[33] Li, B. L.; Zou, H. L.; Tian, J. K.; Chen, G.; Wang, X. H.; Duan, H.; Li, X. L.; Shi, Y.; Chen, J. R.; Li, L. J. et al. Principle of proximity: Plasmonic hot electrons motivate donator-adjacent semiconductor defects with enhanced electrocatalytic hydrogen evolution. *Nano Energy* **2019**, *60*, 689–700.

[34] Wang, S. S.; Jiao, L.; Qian, Y. Y.; Hu, W. C.; Xu, G. Y.; Wang, C.; Jiang, H. L. Boosting electrocatalytic hydrogen evolution over metal-organic frameworks by plasmon-induced hot-electron injection. *Angew. Chem., Int. Ed.* **2019**, *58*, 10713–10717.

[35] Zhang, N.; Han, C.; Fu, X. Z.; Xu, Y. J. Function-oriented engineering of metal-based nanohybrids for photoredox catalysis: Exerting plasmonic effect and beyond. *Chem* **2018**, *4*, 1832–1861.

[36] Linic, S.; Christopher, P.; Ingram, D. B. Plasmonic-metal nanostructures for efficient conversion of solar to chemical energy. *Nat. Mater.* **2011**, *10*, 911–921.

[37] Clavero, C. Plasmon-induced hot-electron generation at nanoparticle/metal-oxide interfaces for photovoltaic and photocatalytic devices. *Nat. Photonics* **2014**, *8*, 95–103.

[38] Su, J.; Feng, L. P.; Zhang, Y.; Liu, Z. T. The modulation of Schottky barriers of metal–MoS_2 contacts via BN–MoS_2 heterostructures. *Phys. Chem. Chem. Phys.* **2016**, *18*, 16882–16889.

[39] Yang, H.; He, L. Q.; Hu, Y. W.; Lu, X. H.; Li, G. R.; Liu, B. J.; Ren, B.; Tong, Y. X.; Fang, P. P. Quantitative detection of photothermal and photoelectrocatalytic effects induced by SPR from Au@Pt nanoparticles. *Angew. Chem., Int. Ed.* **2015**, *54*, 11462–11466.